

# **A PROBABILISTIC FINITE ELEMENT ANALYSIS OF RESIDUAL STRESS FORMATION IN SHRINK-FIT CERAMIC/STEEL GUN BARRELS**

**M. Grujicic and J. R. DeLong**

**Department of Mechanical Engineering  
Clemson University, Clemson SC 29634**

**W. S. DeRosset**

**Army Research Laboratory – Processing and Properties Branch  
Aberdeen, Proving Ground, MD 21005-5069**

**Correspondence to:**

**Mica Grujicic, 241 Engineering Innovation Building, Clemson, SC 29634-0921;  
Phone: (864) 656-5639, Fax: (864) 656-4435, E-mail: [mica.grujicic@ces.clemson.edu](mailto:mica.grujicic@ces.clemson.edu)**

## **ABSTRACT**

The development of residual stresses in a hybrid  $\alpha$ -SiC-lining/CrMoV-steel jacket gun barrel during shrink fitting of the jacket over the lining is studied using a probabilistic finite element analysis. A particular attention is given to understanding the development of the axial compressive stress in the ceramic lining since this stress (if sufficiently high) can prevent lining failure caused by formation and growth of circumferential cracks near the barrel ends. To quantify the effect of variability in various design, materials, and processing parameters on the magnitude and the distribution of the axial residual stress, a probabilistic structural analysis approach, known as the Advanced Mean Value (AMV) method, is used which enables determination of the cumulative distribution function for failure of the lining. The results obtained are validated using the Adaptive Importance Sampling method, an efficient direct statistical sampling technique. Lastly, the corresponding sensitivity factors which quantify the effect of variability in each parameter on the magnitude of axial residual stresses in the ceramic lining are computed. The results indicate that the loss of the compressive axial stress in the lining near the barrel ends is to a greatest extent affected by the magnitude of the friction coefficient at the lining/barrel interface.

---

**Keywords:** ceramic/steel gun barrels, residual stress, probabilistic structural analysis

Report Documentation Page			Form Approved OMB No. 0704-0188		
Public reporting burden for the collection of information is estimated to average 1 hour per response, including the time for reviewing instructions, searching existing data sources, gathering and maintaining the data needed, and completing and reviewing the collection of information. Send comments regarding this burden estimate or any other aspect of this collection of information, including suggestions for reducing this burden, to Washington Headquarters Services, Directorate for Information Operations and Reports, 1215 Jefferson Davis Highway, Suite 1204, Arlington VA 22202-4302. Respondents should be aware that notwithstanding any other provision of law, no person shall be subject to a penalty for failing to comply with a collection of information if it does not display a currently valid OMB control number.					
1. REPORT DATE <b>2002</b>		2. REPORT TYPE		3. DATES COVERED <b>00-00-2002 to 00-00-2002</b>	
4. TITLE AND SUBTITLE <b>A Probabilistic Finite Element Analysis of Residual Stress Formation in Shrink-Fit Ceramic/Steel Gun Barrels</b>			5a. CONTRACT NUMBER		
			5b. GRANT NUMBER		
			5c. PROGRAM ELEMENT NUMBER		
6. AUTHOR(S)			5d. PROJECT NUMBER		
			5e. TASK NUMBER		
			5f. WORK UNIT NUMBER		
7. PERFORMING ORGANIZATION NAME(S) AND ADDRESS(ES) <b>Celmsn University,Department of Mechanical Engineering,Clemson,SC,29634</b>			8. PERFORMING ORGANIZATION REPORT NUMBER		
9. SPONSORING/MONITORING AGENCY NAME(S) AND ADDRESS(ES)			10. SPONSOR/MONITOR'S ACRONYM(S)		
			11. SPONSOR/MONITOR'S REPORT NUMBER(S)		
12. DISTRIBUTION/AVAILABILITY STATEMENT <b>Approved for public release; distribution unlimited</b>					
13. SUPPLEMENTARY NOTES <b>Journal of Materials: Design &amp; Applications, 216 Part L, pp. 219-232, 2002. U.S. Government or Federal Rights License</b>					
14. ABSTRACT <b>The development of residual stresses in a hybrid &amp;#945;-SiC-lining/CrMoV-steel jacket gun barrel during shrink fitting of the jacket over the lining is studied using a probabilistic finite element analysis. A particular attention is given to understanding the development of the axial compressive stress in the ceramic lining since this stress (if sufficiently high) can prevent lining failure caused by formation and growth of circumferential cracks near the barrel ends. To quantify the effect of variability in various design, materials, and processing parameters on the magnitude and the distribution of the axial residual stress, a probabilistic structural analysis approach, known as the Advanced Mean Value (AMV) method, is used which enables determination of the cumulative distribution function for failure of the lining. The results obtained are validated using the Adaptive Importance Sampling method, an efficient direct statistical sampling technique. Lastly, the corresponding sensitivity factors which quantify the effect of variability in each parameter on the magnitude of axial residual stresses in the ceramic lining are computed. The results indicate that the loss of the compressive axial stress in the lining near the barrel ends is to a greatest extent affected by the magnitude of the friction coefficient at the lining/barrel interface.</b>					
15. SUBJECT TERMS					
16. SECURITY CLASSIFICATION OF:			17. LIMITATION OF ABSTRACT <b>Same as Report (SAR)</b>	18. NUMBER OF PAGES <b>37</b>	19a. NAME OF RESPONSIBLE PERSON
a. REPORT <b>unclassified</b>	b. ABSTRACT <b>unclassified</b>	c. THIS PAGE <b>unclassified</b>			



## **I. INTRODUCTION**

**It is generally accepted that future war fighting and peacekeeping operations of the US Armed Forces will entail rapid deployment of light air-mobile vehicles with large caliber guns capable of providing increased range, accuracy, and energy on target. According to Katz [4], conventional CrMoV-based gun steels are at their limit with respect to the ability to withstand thermal cracking and/or melting-erosion induced during long-burst firing of the large diameter guns. Thus, to achieve the aforementioned range, accuracy and impact-energy objectives, new generations of advanced guns that can fire ammunition using advanced high-energy propellants, will have to be developed. This will require the use of new materials and design strategies, which can provide increased high-temperature operational capabilities and improved erosion resistance [1].**

**One of the approaches to enhancing the performance of large-caliber guns is the use of hybrid gun barrels consisting of a ceramic lining and a steel jacket. Due to their high melting temperature (controls melting-erosion resistance), high hot-hardness (controls wear and erosion resistance), and chemical inertness (controls corrosion-erosion resistance), ceramics appear as quite attractive materials for gun-barrel liner applications. However, ceramics suffer from a lack of fracture toughness and tensile strength, which may hinder their use in advanced gun barrels [2,3].**

**A review of the literature [1] reveals that three types of ceramic linings:  $\alpha$ -SiC, Si<sub>3</sub>N<sub>4</sub> and SiAlON (a Si<sub>3</sub>N<sub>4</sub> + Al<sub>2</sub>O<sub>3</sub> solid solution) are capable of surviving only 1000 rounds in the single-shot firing mode and only 100 rounds in the burst-firing mode of conventional ammunition with a standard M2 propellant in .50 caliber machine guns. The primary failure mode in these barrels is formation and growth of circumferential cracks near the ends of the ceramic insert. Since the ceramic lining is initially placed in a triaxial compressive stress state by shrink fitting the steel jacket over it, the observed failure mode is believed to be the result of a reduction (or a complete loss) of axial compression in the lining due to slippage at the lining/barrel interface near the barrel ends.**

Only  $\alpha$ -SiC liners have so far been tested in single-shot and burst-firing modes using specially designed ammunition and a JA-2 high-energy propellant (flame temperature  $\sim 3450\text{K}$ ) in a 25 mm bore gun barrel. This propellant gives rise to a  $\sim 17\%$  increase in the projectile velocity at the muzzle-end of the barrel relative to that attained using the standard M2 propellant. These  $\alpha$ -SiC linings also suffered from formation of multiple circumferential cracks near the breach and the muzzle ends of the barrel with the first crack being observed after the initial 20-round burst. An important observation was made that while each end of the linings was converted to a stack of washers, the cracks were “tight” (no evidence of gas leakage to the steel jacket was found) and they did not apparently degrade the gun performance significantly. In fact, testing was terminated due to excessive erosion of a CrMoV steel gun-barrel extender and not due to lining degradation. These observations suggest that the loss of axial compression in the ceramic lining caused by slippage at the lining/jacket interface near the barrel ends during the shrink-fit process, is a very critical step in the circumferential-cracks formation process. During long-burst firing the temperature of the steel jacket increases substantially. As the jacket expands, it pulls on the adjoining ceramic lining. Unless the compressive residual stress in the lining is sufficiently high, this can give rise to a high tensile stress and cracking in the lining near the barrel ends. When firing stops, the steel jacket begins to cool and restores the compressive residual stresses in the lining ensuring structural integrity of the barrel [4].

The objective of the present work is to carry out a probabilistic finite element analysis of the development of residual stresses in a 25mm-bore hybrid  $\alpha$ -SiC lining/CrMoV-steel jacket gun barrel during a shrink-fit process. Analyses of residual stresses by a finite element method are generally done using a deterministic scheme in which nominal values are used for geometrical, material, and process parameters. Since these parameters are not generally known with an absolute certainty, a probabilistic finite element approach is used in the present work to assess statistical variability of the residual stresses and their sensitivity to variation in different design, material, and process parameters. A performance analysis of hybrid gun barrels during single-shot and burst-firing events has been presented in our recent paper [5].

The organization of the paper is as follows. A brief overview of the probabilistic structural analysis methods used is presented in Section II.1. A detailed description of the finite element procedure used to analyze the development of residual stresses during the shrink-fit process is given in Section II.2. Main results obtained in the present study are presented and discussed in Section III. Key conclusions resulting from the present work are summarized in Section IV.

## II. COMPUTATIONAL PROCEDURES

### II.1. Probabilistic Structural Analysis

The structural reliability analysis is based on the concept of a limit-state or failure function [6-10]. The limit-state function  $g(X)$  is a function of a vector of basic random (design) variables,  $X=(X_1, X_2, \dots, X_n)$ , with  $g(X)=0$  defining the limit-state surface. The limit-state surface separates the design space into two regions: a failure region in which  $g(X) \leq 0$  and a safe region in which  $g(X) > 0$ . The limit-state function is generally defined as:

$$g(X) = Z(X) - z_0 = 0 \quad (1)$$

where  $Z(X)$  is a response or a performance function of the system being analyzed and  $z_0$  is a critical value of the response (performance) function.

For the given joint probability density function of the design variables,  $f_x(X)$ , the probability of failure is defined as:

$$P_f = \int_{\Omega} \dots \int f_x(X') dX' \quad (2)$$

where  $\Omega$  denotes the failure domain. Computation of the failure probability by direct evaluation of the multi-dimensional integral in Equ. (2) can be difficult for complicated failure functions but can be straightforward using a standard Monte Carlo procedure.

The Monte Carlo simulation method involves random sampling of each design variable according to its distribution followed by evaluation of the system performance function. For correlated variables, the sampling has to be adjusted to take into account the correlations. Design variables sampling and subsequent performance function

evaluations are repeated until sufficiently large number of  $Z(X)$  values is obtained from which the statistics of the response can be determined. The main strength of the Monte Carlo method is that it is exact in the limit of a very large number of samples.

However, the method has a serious disadvantage in that a very large number of function evaluations may be necessary, particularly when very rare events need to be captured. A typical rule of thumb specifies the minimum number of function evaluations needed for low failure probabilities  $P_f$  as greater or equal to  $10/P_f$ .

Conversely, for the failure probability nearing one, the number of simulations needed is no less than  $10/(1 - P_f)$ .

In most structural applications, the acceptable probability of failure is quite small. Therefore, the number of necessary function evaluations becomes very high, of the order of tens or hundreds of thousands. When the computation of the performance function is time consuming (e.g. it entails extensive finite element computations), the use of the Monte Carlo method becomes prohibitively expensive. Under such circumstances, advanced-approximate probabilistic methods that can compute the probabilistic response with far fewer number of function evaluations have to be utilized. In the present work, the Advanced Mean Value method developed by Millwater and co-workers is used [6-10].

### II.1.1 Advanced Mean-Value Method

The Advanced Mean Value (AMV) method provides a bridge between a crude Mean Value (MV) based analysis and an accurate Monte Carlo method-based analysis of the cumulative probability distribution function [11]. It is, in general, a substantially more accurate method than the MV method with a minor increase in the number of calculations required.

Within the MV method, a performance function,  $Z(X)$ , of the system being analyzed is approximated using the following truncated Taylor series:

$$Z_{MV} = Z(\mu_x) + \sum_{i=1}^n \left( \frac{\partial Z}{\partial X_i} \right) \cdot (X_i - \mu_i) = a_0 + \sum_{i=1}^n a_i X_i \quad (3)$$

where the derivatives  $(\partial Z / \partial X_i)$  are evaluated at the mean values  $\mu_i$  of the design variables  $X_i$  ( $i=1, \dots, n$ ), and  $\mu_x$  is used to denote a vector containing the mean values of the design variables. These derivatives are readily calculated by numerical differentiation. Within the advanced mean-value model, the MV-based performance function is corrected as:

$$Z_{AMV} = Z_{MV} + H(Z_{MV}) \quad (4)$$

where  $H(Z_{MV})$  is defined as a (negative) difference between the approximate performance-function values  $Z_{MV}$  (obtained using Equation (3)) and the accurate performance-function values (calculated using the function  $Z(X)$  defined in Equation (1)), along the locus of the most probable points (MPPs) at different levels,  $z_0$ , of the system response. The most probable point at a given response level is defined as the point with the maximum joint probability density of the design variables.

Determination of the most probable point is generally done in a space defined by independent standard-normal random variables. If the random variables  $X_i$  are mutually dependant they have to be first transformed into a set of independent variables as discussed in Ref. [12]. In the present work, all the random design variables  $X_i$  selected are mutually independent. Each of the variables, which is not a standard normal variable should be transformed into the standard normal values,  $u_i$  using the following transformation:

$$\Phi(u_i) = F_x(X_i) \quad \text{or} \quad u_i = \Phi^{-1}[F_x(X_i)] \quad (i=1, \dots, n) \quad (5)$$

where  $\Phi$  is the cumulative probability distribution function for the standard normal distribution. The system performance function  $Z(X)$  is then converted into the corresponding  $Z(u)$  function. The most probable point in the  $u$ -space at any level of system response  $Z(u) = z_0$  is the point on the  $g(u) = Z(u) - z_0$  limit-state surface located at the minimum distance (denoted as  $\beta$ ) from the space origin ( $u=0$ ). To help clarify the most probable point concept, a case involving two random variables is shown schematically in Figure 1.

The locus of the most probable points for different levels of the system performance  $z_0$  can be determined by solving the following optimization problem:



minimize the magnitude of the vector  $u$ ,  $|u|$ , subject to the constraint that  $Z(u) = z_0$  which can be accomplished by various optimization algorithms [e.g. 13]. Within the AMV method, this optimization procedure is carried out in such a way that the approximate mean value function  $Z_{MV}$ , Equation (3), is used as the constraining equation  $Z_{MV}(u) = z_0$ . Since this does not involve costly (e.g. finite element base) evaluations of the system performance, determination procedure for the MPP is highly efficient. Once the most probable point in the  $u$ -space,  $u^*$ , is found, the corresponding most probable point in the  $X$ -space,  $X^*$ , is obtained by inverting the transformation given in Equation (5).

The accuracy of the AMV solution obtained depends on the correctness of the mean-value based locus of the most probable points. To further improve the advanced mean-value solution at a given level of the system response  $z_0$ , the so-called AMV+ method is used. Within this method, the response function is approximated around the most probable point,  $X^*$ , using the following truncated Taylor series:

$$Z_{MPP} = Z(X^*) + \sum_{i=1}^n \left( \frac{\partial Z}{\partial X_i} \right) \bigg|_{X^*} (X_i - x_i^*) = b_0 + \sum_{i=1}^n b_i X_i \quad (6)$$

Equation (6) is next used as a constraining equation in the optimization procedure discussed above to update the most probable point corresponding to a given level of system response. Lastly, the accurate (e.g. finite element base) response function is used to evaluate the system response at the updated value of the most probable point.

To summarize, the AMV and AMV+ methods involve the following steps:

(1) The MV response function approximation is first constructed using Equ. (3) and used in conjunction with a sampling scheme to evaluate the “mean-value based” cumulative distribution function of the system response. As shown in Table 1, this step entails  $n$  evaluations of the accurate system response function, where  $n$  is the number of random variables.

(2) For a given level of the cumulative distribution function, the constrained optimization procedure is used to determine the most probable point  $X^*$  and, in turn,

accurately evaluate the corresponding system response  $Z(X^*)$ . As shown in Table 1, this step requires only one additional evaluation of the accurate response function.

(3) To further improve the AMV solution at a given level of the cumulative distribution function, design variables are perturbed around  $X^*$  and Equ. (6) used to construct  $Z_{MPP}$ . After the cumulative distribution function is determined via the sampling scheme discussed above, Equ. (6) is used as the constraining equation in the optimization procedure to update the most probable point ( $X^{**}$ ) and the system response is reevaluated one more time as  $Z_{AMV+} = Z(X^{**})$ . As shown in Table 1, this step requires  $n+1$  accurate performance function evaluations.

(4) Step 3 is repeated until convergence of the system performance is reached for a given level of the cumulative distribution function.

When the limit state surface can not be well represented using the truncated Taylor series or other low order polynomials, the AMV+ based solution for the failure probability may be inaccurate. In such cases, an efficient direct-sampling scheme is needed to verify the AMV+ based solution. One such scheme, the Adaptive Importance Sampling method, appears to be particularly efficient and is employed in the present work [6,10].

### II.1.2 Adaptive Importance Sampling Method

The Adaptive Importance Sampling (AIS) method has two salient features: (a) design-variables sampling within the safe region is minimized and instead it is concentrated in the portion of the failure region in which the failure probability is highest and; (b) the sampling region is continuously increased in the course of sampling by properly deforming the boundary of the sampling region until the sampling region completely covers the failure region, at which point the probability of failure converges [6,10].

The first step in this sampling procedure involves introduction of an approximate sampling (limit-state) function  $g_s(u)$  in the (standard-normal)  $u$ -space which is typically defined as a full second-order Taylor expansion around the most probable point ( $u^*$ ) as:

$$g_s(u) = \nabla g_s(u^*)^T (u - u^*) + \frac{1}{2} (u - u^*)^T D(u^*) (u - u^*) \quad (8)$$

where  $g_s(u^*) = 0$ ,  $\nabla g_s(u^*)$  is the gradient vector, and  $D$  a symmetric matrix of the partial second-order derivatives:

$$D_{ij}(u^*) = \frac{\partial^2 g_s(u^*)}{\partial u_i \partial u_j} \quad (9)$$

The gradient vector and the matrix  $D$  are computed using a finite difference method and either the AMV+ based or the exact (finite element based) performance function evaluations. To simplify the computation of the failure probability for the (original) limit-state function, Equ. (8), the following orthogonal transformation [12,14-15] is first employed:

$$u = -H^T v \quad (10)$$

where the  $n$ -th row of the matrix  $H$  contains the sensitivity factors,

$$\alpha_i^* = \left( \frac{\partial g_s}{\partial u_i} \right) \Big|_{u^*} / \|\nabla g_s(u^*)\| = -u_i^* / \beta, \text{ evaluated at } u^*. \text{ This orthogonal}$$

transformation thus aligns the  $v_n$  variable with the vector connecting the space origin with the MPP. The components of the MPP in the  $v$ -space are therefore

$$v_i^* = 0 \ (i=1, \dots, n-1), \ v_n^* = \beta \text{ and Equ. (8) can then be rewritten as:}$$

$$g_s(v) = \beta - v_n + \frac{1}{2 \|\nabla g_s(u^*)\|} v^T H D H^T v \quad (11)$$

where  $\beta (= u^{*T} u^*)$  is the distance of the most probable point from the  $v$ -space (or  $u$ -space) origin and the vector  $v$  is defined in Equ. (8) as:

$$v = (v_1, v_2, \dots, v_n - \beta) \quad (12)$$

Equ. (11) represents a general second-order  $n$ -dimensional surface and can be further simplified if, in the second term on the right-hand side of this equation, only the

second-order terms for  $v_i$  ( $i=1,2,\dots,n-1$ ) are retained, resulting in the following hyperbolic function [23]:

$$g_s(v) = \beta - v_n + v^T A v \quad (13)$$

where now  $v=(v_1, v_2, \dots, v_{n-1})$  and

$$A_{ij} = \frac{(HDH^T)_{ij}}{2|\nabla g_s(u^*)|}, \quad i, j = 1, \dots, n-1 \quad (14)$$

Next, a second orthogonal transformation is used to diagonalize matrix  $A$  as:

$$v = H_1 w \quad (15)$$

where matrix  $H_1$  contains eigenvectors of matrix  $A$  as column vectors. This transformation converts Equ. (13) into:

$$g_s(v, w) = \beta - v_n + \frac{1}{2} \sum_{i=1}^{n-1} k_i w_i^2 \quad (16)$$

where  $k_i=2\lambda_i$  represents the  $i$ -th principal curvature and  $\lambda_i$  is the corresponding eigenvalue of matrix  $A$ . To further simplify the failure function, the individual curvatures appearing in Equ. (16) are replaced with a single (asymptotic second-order reliability method-based [15]) curvature defined as:

$$k_M = \frac{1}{\beta} \left[ \prod_{i=1}^{n-1} (1 + \beta k_i)^{1/2} - 1 \right]^{n-1}. \quad (17)$$

This allows for Equ. (16) to be rewritten as:

$$g_s(v, w) = (\beta - v_n) + \frac{1}{2} k_M \sum_{i=1}^{n-1} w_i^2 \quad (18)$$

Equ. (18) defines a parabolic form of the limit-state function in a coordinate system defined by  $v_n$  (colinear with a line connecting the space origin with the MPP in Figure 2) and  $n-1$   $w_i$ 's (tangent to the limit state surface at the MPP). Examination of Equ. (18) reveals that since  $v_n$  and  $w_i$  ( $i=1, \dots, n-1$ ) are uncorrelated standard normal

variables, the second term in this equation has a Chi-square distribution with  $n-1$  degrees of freedom while the first term has a standard normal distribution.

If a new random variable  $s^2 = \sum_{i=1}^{n-1} w_i^2$  is introduced to handle the second term in Equ. (18), the probability density function for the failure function  $g_s$  can be defined as:

$$f_g(g_s) = \int_0^\infty f_v(\beta - g_s + \frac{1}{2}k_M s^2) f_{s_{n-1}^2}(s^2) ds^2 \quad (19)$$

where  $f_v()$  and  $f_{s_{n-1}^2}()$  refer respectively to the standard normal and the  $(n-1)$  degree of freedom) Chi-square probability density functions. The failure probability (the probability that  $g_s \leq 0$ ) based on the probability density function defined by Equ. (19) can then be expressed as:

$$P_f = \int_{-\infty}^0 f_g(g_s) dg_s = \int_0^\infty \Phi(\beta + \frac{1}{2}k_M s^2) \cdot f_{s_{n-1}^2}(s^2) ds^2 \quad (20)$$

The probability density function for random variable sampling within the failure region bounded by Equ. (18) is then defined as:

$$f_{s^2}(s^2) = \frac{\Phi\left(\beta + \frac{1}{2}k_M s^2\right) \cdot f_{s_{n-1}^2}(s^2)}{P_f} \quad (21)$$

This function can be constructed numerically for the given  $\beta$ ,  $k_M$  and  $n$  and the  $s^2$  variable sampled by first generating a random number  $r$  distributed uniformly in the range (0,1) and then using the method of inversion of the cumulative distribution function to compute  $s^2$  as [16]:

$$s^2 = F_{s^2}^{-1}(x) \quad (22)$$

where  $F_{s^2}()$  is the cumulative distribution function corresponding to the probability density function given by Equ. (21). Once  $s^2$  is selected, a random angle in a range from 0 to 180 degrees is chosen and used to define the directional cosine of one of  $w_i$ 's

( $i=1, \dots, n-1$ ) and the remaining  $w_i$ 's are calculated so that the condition  $s^2 = \sum_{i=1}^{n-1} w_i^2$  is satisfied. The random variable  $v_n$  is next selected from the standard normal distribution so that  $v_n \geq \beta + k_M \sum_{i=1}^{n-1} w_i^2$  which guarantees that the sampled point is within the failure region. The sampled design point with the coordinates  $w_i$  ( $i=1, \dots, n-1$ ),  $v_n$  is next transformed to its corresponding  $u$ -space point using  $H_I$  and  $H$  matrices, and then transformed to its  $X$ -space point. The exact limit-state function  $g(X)$  is next computed in order to determine its sign i.e. whether the sampled point is in the failure or the safe region.

## II.2 Finite Element Analysis

### II.2.1 Description of the Problem

A schematic of a gun-barrel assembly used for testing  $\alpha$ -SiC barrel liners under single-shot and burst firing condition is shown in Figure 3. The barrel is 355.6mm long, has a 25.0mm bore and the  $\alpha$ -SiC lining is 3.175mm thick. The wall thickness of the steel jacket is approximately 25.4mm. As shown in Figure 3, the barrel assembly also includes a (non-lined) steel barrel extender and a steel shank. Minor components in the barrel assembly such as set screws, compliant washers and a seal are not shown to keep the figure simple. Also a 0.15mm thick lining/jacket compliant interlayer made of copper (often employed to reduce point-type contact stresses at the liner/jacket interface) is not shown. Since point-type contact stresses (controlled by roughness of the contacting surfaces) are not modeled within the present work, the compliant copper layer is not considered.

As discussed earlier, in order to attain a triaxial compressive stress state in the ceramic lining, the steel jacket is typically placed over it using a shrink-fit process. Within this process, the jacket is heated to a sufficiently high temperature in order to expand its bore and slid over the tubular ceramic lining. Since the (ambient temperature) ceramic-lining outer diameter is larger than the (ambient temperature) steel-jacket inner diameter, the lining prevents a complete contraction of the jacket during cooling and the resulting hybrid ceramic/steel tube develops residual stresses. In particular, since the steel jacket is prevented from fully contracting by the ceramic

lining, it acquires a tensile stress state. Conversely, compressive residual stresses develop in the ceramic lining. Since the ability of ceramics to withstand compressive stresses is at least an order of magnitude higher than their tensile strength, it is generally desirable to maximize the level of compressive residual stresses in the lining. The maximum achievable level of residual stresses in ceramic linings is typically limited by at least two factors: (a) high (tensile) contact stresses at the ceramic/steel interface, if substantially higher than 500MPa, can lead to crack formation in the ceramic lining and; (b) the maximum temperature to which the steel jacket is heated (which controls the level of residual stresses) is limited to 1200K by the requirement that no significant changes in the steel microstructure take place during the shrink fit process. In addition, as discussed earlier, slippage at the ceramic/steel interface near the tube ends gives rise to a reduction of compressive residual stress in the ceramic lining and can have a profound effect on the performance of hybrid ceramic/steel gun barrels.

The problem of development of the compressive residual stresses during a shrink-fit process and, in particular, a loss of the axial compressive residual stress in the ceramic lining near the barrel ends and its sensitivity to variability in design, materials and process parameters are studied in the present work by carrying out a series of combined thermal/stress finite element analyses using the commercial finite element package ABAQUS/Standard [17].

## **II.2.2 Formulation of the Problem**

Development of the residual stresses during the shrink-fit process is modeled in two steps: (a) a transient heat transfer analysis and (b) an elastic-plastic mechanical stress analysis. Decoupling the study in the separate thermal and mechanical analyses is justified since, due to a low extent of plastic deformation in the tube, the contribution of the plastic strain energy dissipated as heat to the energy conservation equation is expected to be minimal while the effect of temperature on materials mechanical properties can be incorporated directly in the mechanical analysis.

A schematic of the model used in the thermal analysis is shown in Figure 4(a). In the initial condition, the steel jacket is set at a temperature of 1173K in order to comply with the experimental procedure described in reference [4], while the ceramic liner is

held at room temperature (298K). A heat transfer by conduction is considered to take place throughout the solid material while heat exchange between the solid and the surrounding is taken to be controlled by convection and radiation.

A schematic of the model used in the mechanical analysis is shown in Figure 4(b). In the initial condition, the ceramic lining and the steel jacket are both stress-free and each at its respective initial temperature. As time progresses, differences in temperatures and thermal expansion coefficients give rise to formation of residual stresses.

Initial calculations in which full-length tubes were used showed that variations in the residual stress with distance along the tube axis occur only to about 70mm away from the tube ends. Hence, all the calculations reported in the present work involved shortened, 152.4mm-long tubes. Furthermore, a symmetry conditions is applied in the length (z) direction so that only a half of the barrel had to be modeled. The finite element mesh used in both thermal and mechanical analyses is shown in Figure 4(c). The computational domain is partitioned into 864 eight-node quadrilateral axisymmetric elements (DCAX8 ABAQUS elements for the thermal analysis and CAX8 ABAQUS elements for the mechanical analysis). Since high-gradients of the residual stresses are localized to a region adjacent to the lining/jacket interface and near the tube ends, mesh refinement is employed in these regions.

The mean-value and the standard deviation data for the (thermal and mechanical) materials properties and the process parameter (steel-jacket temperature) used in the present finite element analyses are given in Table 2. Variability of all parameters considered is assumed to be governed by the appropriate normal distribution. The materials properties listed in Table 2 are obtained from the commercial materials database Cambridge Engineering Selector [18]. The effect of variability of one shrink-fit process parameter, the initial temperature of the steel jacket , is also considered.

### III. RESULTS AND DISCUSSION

Contour plots of the temperature distribution in the hybrid  $\alpha$ -SiC/CrMoV-steel barrel at three different cooling times (0.01s, 1.0s and 100.0s) are shown in Figures 5(a)-



5(c), respectively. These results are obtained using the mean values of all thermal material parameters listed in Table 2. The results shown in Figures 5(a)-5(c) are as expected. That is, since only the steel jacket is initially at a high temperature, once the jacket is slid over the lining, the lining begins to heat while the jacket cools both due to heat conduction to the lining and due to heat convection/radiation to the surrounding, Figure 5(a). Furthermore, due to a relatively high thermal conductivity of  $\alpha$ -SiC and a low mass of the lining compared to that of the jacket, the lining quickly heats up and reaches temperatures comparable to those in the jacket, Figure 5(b). During further cooling, both the lining and the jacket undergo a temperature decrease. Due to heat exchange with the surrounding through the tube surfaces, the highest temperatures are found in the interior of the tube, Figure 5(c). Furthermore, since the surface area through which heat is exchanged with the surrounding is considerably smaller for the lining than for the jacket, the highest temperature region shifts toward the ceramic lining as cooling proceeds, Figure 5(c).

Contour plots of the axial, radial, and circumferential residual stresses in the hybrid ceramic/steel gun barrel at the completion of the shrink-fit process (when the temperature of the entire hybrid barrel becomes equal to the ambient temperature) are shown in Figures 6(a)-6(c), respectively. These results are also obtained using the mean values of the materials and the processing parameters. A simple examination of the results shown in Figures 6(a)-6(c) reveals that almost the entire  $\alpha$ -SiC lining is subject to a triaxial compressive stress state. A small region at the lining end experiences tensile radial stress whose magnitude ( $<70\text{MPa}$ ) is quite small compared to the magnitudes of the compressive axial and tangential stresses in the same region.

Contour plots displaying evolution of the residual axial stress during the shrink-fit process are shown in Figures 7(a)-(c). The cooling times (.01s, 1.0s, and 100.0s) in Figures 7(a)-(c), respectively are selected to be identical to those associated with Figures 5(a)-(c) in order to reveal the relationship between the temperature field and the axial stress field. At the shortest time displayed (0.01s), the temperature changes relative to the initial temperatures of the lining and the steel jacket and, hence, the (thermal) stresses are primarily located near the lining/jacket interface, Figures 5(a) and 7(a). As

cooling proceeds, the temperature of the ceramic lining becomes more comparable to that of the steel jacket, Figures 5(b)-5(c) and, due to a lower coefficient of thermal expansion, the ceramic lining begins to develop a compressive axial stress while the steel jacket experiences axial tension, Figures 7(b)-(c). This process continues with cooling, giving rise to increasingly higher levels of the axial stress in the region near the right (symmetry) end of the barrel. However, at the same time, slippage at the lining/barrel interface near the free end of the tube gives rise to a significant reduction in the magnitude of the compressive axial stress, Figures 7(b) and (c).

Since the reduction of the axial compressive stress in the ceramic lining near the barrel ends due to a slip at the lining/jacket interface has been identified [1] as one of the key factors promoting failure of the gun-barrel linings during burst firing by formation and growth of circumferential cracks and since such cracks are believed to originate at the lining/jacket interface, the distribution of the axial stress  $\sigma_{zz}$  in the lining along the lining/jacket interface is analyzed, Figure 8. The results displayed in Figure 8 show that indeed the axial residual stress is reduced in the lining near the tube end and that the magnitude of this stress decreases continuously (to zero) as the tube end is approached.

To analyze the effect of variability in materials and process parameters on the performance of the  $\alpha$ -SiC barrel lining, the performance function is defined, in the present case, as the Weibull probability for failure of the lining when it is subject to a uniform axial tensile stress equal to the tensile strength of  $\alpha$ -SiC (generally reported as 450MPa). Since the dominant mode of failure in ceramic linings is formation and growth of circumferential cracks at the lining/jacket interface near the barrel ends, it is assumed that lining failure is initiated by surface flaws and that it is governed by the axial stress alone. Hence, the probability for failure (the performance function) is defined as [24]:

$$Z(X) = P_f(X) = 1.0 - \exp - \int_0^{l_i} \left( \frac{\sigma_{app} - \sigma_{zz}(X, z)}{\sigma_0} \right)^m \cdot 2\pi r_i \cdot dz \quad (23)$$

where the vector  $X$  contains all the material/process variables listed in Table 2,  $\sigma_{app}=450\text{MPa}$ ,  $\sigma_o$  ( $=556\text{MPa}$  [25]) is the scaling factor which is numerically equal to the stress level at which  $P_f=0.632$  in a material of a unit volume,  $\sigma_{zz}(X,z)$  is the axial stress in the row of elements of the ceramic lining adjacent to the steel jacket,  $m$  ( $=6.59$  [25]) is the Weibull modulus,  $r_l$  ( $=15.675\text{mm}$ ) is the outer lining radius,  $l_l$  ( $=76.3\text{mm}$ ) is the barrel length and  $z$  is a measure of the distance along the barrel length. Enumeration of the components of the vector  $X$  is given in Table 3.

To construct the MV-based approximation,  $Z_{MV}(X)$ , for  $Z(X)$  using Equ. (3), each random variable  $X_i$  is perturbed by 0.1 of its standard deviation and a first-order finite difference procedure used to compute the partial derivatives  $\partial Z / \partial X_i |_{\mu}$ . The values of the Taylor series coefficients,  $a_i$ , appearing in Equ. (3) are listed in Table 3. The corresponding normalized sensitivities of the performance function to small variations in the material and process parameters relative to their mean values, defined as  $\alpha_i = \partial Z / \partial u_i |_{\mu_x} = \sigma_i \partial Z / \partial X_i |_{\mu_x}$ , are also listed in Table 3. The  $\alpha_i$  values listed in Table 3 indicate that the friction coefficient at the lining/jacket interface has the dominant effect on the extent of reduction of compressive axial stress near the barrel end and hence on the failure probability of the lining. Among other parameters, the thermal expansion coefficient and the yield strength of the steel and the Young's modulus and the thermal expansion coefficient of  $\alpha$ -SiC have largest effects.

Once  $Z_{MV}$  function is determined, 10,000,000 design points are generated by randomly sampling each variable  $X_i$  using its probability distribution function and, for each design point,  $Z_{MV}$  is evaluated using Equ. (3). A frequency map for  $Z_{MV}$  is next constructed and used to compute the corresponding cumulative distribution function, CDF. The results of this procedure are shown in Figures 9(a) and (b). A conventional linear CDF scale is used along the vertical axis in Figure 9(a). On the other hand, a normal-distribution CDF scale with a number of standard deviations as unit is used along the left vertical axis in Figure 9(b). The corresponding CDF probability levels are denoted along the right vertical axis in Figure 9(b).

The results shown in Figure 9(a) indicate that there is a small ( $<0.0009$ ) probability for the lining to be failure-proof (i.e. for its failure probability to be zero). Furthermore, the linear nature of the  $Z_{MV}$  plot shown in Figure 9(b) indicates that the system performance (the failure probability of the lining) has a normal distribution. This finding is expected since variability of all the material/process variables  $X_i$  is also governed by normal distributions. It is also seen that when the materials and process parameters are set to their mean values (CDF=0.5 in Figure 9(a)), the failure probability is approximately 0.005 (i.e. the lining is expected to fail in 5 out of 1,000 barrels). While, this level of failure probability can be considered as already high, the limiting value for the performance function is defined as  $P_f(X) = 0.01$  [19]. The results shown in Figure 9(b) indicate that the MV-based probability for  $P_f(X) \geq 0.01$  is quite small ( $\sim 0.0008$ ), Point A in Figure 9(b).

To determine the most probable point corresponding to the  $Z(X) = P_f(X) = 0.01$ , each design variable  $X_i$  is first transformed into the corresponding standard normal variable  $u_i$  using Equ. (5). Since all the random variables, in the present case, are normal variables, Equ. (5) acquires a simple form:  $u_i = (X_i - \mu_i) / \sigma_i$  where  $\mu_i$  and  $\sigma_i$  are the mean value and the standard deviation, respectively. The Simplex method [20] is next used to find the MPP,  $u^*$ , by solving the optimization problem: minimize  $|u|$  subject to  $Z_{MV}(u^*) = 0.01$ . The corresponding MPP in the  $X$ -space,  $X^*$ , is then determined by the following inverse transformation:  $X_i^* = \sigma_i u_i^* + \mu_i$  and the finite element analysis used to compute  $Z(X^*) = P_f(X^*)$  at the same level of the cumulative distribution function of 0.0008, Point B in Figure 9(b). This procedure yields  $Z(X^*) = P_f(X^*) = 0.0266$ . Since this value is considerable different from the MV-based value,  $P_f(X) = 0.01$ , it appears that the performance function  $Z(X)$  is quite nonlinear and the use of the (linear) Taylor series expansion around the MV point leads to substantial inaccuracies in evaluation of  $Z(X)$ . These inaccuracies are subsequently removed using the AMV+ procedure. It should be also noted that to distinguish between the  $Z(X)$  values evaluated using the Taylor series expansion and the ones obtained using the finite element calculation, the former are denoted as solid

circles (e.g. Point A in Figure 9(a)) while the latter using solid squares (e.g. Point B in Figure 9(b)).

To improve the accuracy of evaluation of the performance function, the AMV+ method is employed. Toward that end, all random variables are perturbed around the MPP point,  $\partial Z / \partial X_i|_{X^*}$  derivatives evaluated using a finite difference method and the  $Z_{MPP}$  function (solid line in Figure 9(b)) determined using Equ. (6). It is seen that employing the AMV+ method increases the probability for  $P_f(X) \geq 0.01$  to  $\sim 0.0020$ , Point C in Figure 9(b) relative to its MV-based value (0.0008, Point A in Figure 9(b)). Next, the MPP finding procedure is repeated while using the  $Z_{MPP}$  function as the constraining equation and the performance function recomputed (as  $P_f=0.164$ ) at the updated MPP using the finite element method, Point D in Figure 9(b).

To satisfied the imposed convergence condition (magnitude of the relative change in the finite-element based value for  $Z(X)$  between two adjacent iterations is less than 0.05), the AMV procedure had to be repeated two more times. The results of the first of these iterations are displayed as Pints E and F in Figure 9(b). The final solution in denoted by Point G in Figure 9(b) and shows that the probability for  $P_f(X) \geq 0.01$  is approximately 0.0064.

To validate the AMV+ finding presented above, the Adaptive Importance Sampling (AIS) method discussed in Section II.1.2 is employed. Toward that end, each standard-normal random variable  $u_i$  is perturbed in both directions around the MPP corresponding to Point G in Figure 9(b), the first- and second-order finite difference methods used to determine the gradient vector,  $\nabla g_s(u^*)$ , and the matrix of second-order partial derivatives,  $D$ , and, in turn, Equ. (8) employed to construct the initial limit-state (sampling) function  $g_s(u)$ . Next the sensitivities  $\alpha_i$ 's at the MPP are computed as  $\alpha_i = -u_i^* / \beta$  where  $\beta = |u^*|$  and used as elements of the last column (column 19) of the matrix  $H$ , Equ. (10). The remaining elements of the matrix  $H$  are selected in such a way that the orthogonal character of the matrix is achieved. Next, the matrix  $H$  is redefined as the upper left (18x18) minor matrix of the original matrix  $H$  and the matrix  $A$  computed using Equ. (14). Eigenvalues  $\lambda_i$  ( $i=1, \dots, 18$ ) and the

corresponding eigenvectors of the matrix  $A$  are next determined and used to compute the principal curvatures  $k_i=2\lambda_i$  and, in turn, to construct the matrix  $H_I$ . Lastly, Equ. (17) is employed to compute the mean curvature  $k_M$  and the values of  $\beta$  and  $k_M$  used to determine both the probability density function for random variables sampling from the failure-region, Equ. (21) and the corresponding failure probability, Equ. (20).

Since the number of random variables in the present case is relatively large ( $n-1=18$ ), the chi-square density distribution function with  $n-1=18$  degrees of freedom in Eqs. (20) and (21) is simplified by replacing it with a normal distribution function with a mean equal to  $n-1=18$  and a variance equal to  $2(n-1)=36$ . By numerically integrating Equ. (20) using the procedure outlined in Ref. [22], the probability for a randomly selected point to fall in the unsafe (failure) region as defined by the initial limit-state function is found to be  $P_{0,1} = 0.0079$ .

The AIS method is initiated by sampling  $N_{s,1}=10$  points of the random variable  $s^2$  in accordance with the probability density function given by Equ. (21) using the method of inversion of the (corresponding) cumulative distribution function, Equ. (22). Each sampled  $s^2$  point and a randomly selected angle are then used to determine the corresponding 18 standard normal variables  $w_i$  so that  $s^2 = \sum_{i=1}^{18} w_i^2$ . Also, the random variable  $v_{19}$  is selected from the standard normal distribution so that  $v_{19} \geq \beta + k_M s^2$  which ensures that the sampled point is within the failure region as defined by the initial limit-state (sampling) function. Each sampled design point defined by the random variables  $w_i (i=1, \dots, 18)$  and  $v_{19}$  is next first transformed to its corresponding point in the  $u$ -space using the matrices  $H_I$  and  $H$ , and subsequently to the corresponding point in the  $X$ -space. The finite element method is then used to determine the sign of the limit-value function  $g(X)=Z(X)-0.01$ , i.e. to find out whether the sampled point is in the failure region or in the safe region.

Out of 10 points initially sampled,  $N_{f,1}=9$  are found to fall within the failure region. The probability for a randomly selected point to fall in the failure region is next updated as:  $P_{f,1} = P_{0,1} \cdot N_{f,1} / N_{s,1} = 0.079 \cdot 9/10 = 0.0071$ . The  $R=N_f/N_{11}=0.9$  ratio is next used to determine the total initial number of random points which need to be

sampled,  $N_{st,1}$ , in order to compute the failure probability within an error  $\gamma \leq 0.10$  and with a confidence level  $1 - \alpha \geq 0.90$  as:  $N_{st,1} = (1 - R) \cdot R \cdot [\Phi^{-1}(1 - \alpha / 2) / (\gamma \cdot R)]^2 = 30$  [21]. Next, additional  $N_{st,1} - N_{s,t} = 20$  points are sampled and the failure probability recomputed as:  $P_{f,1} = P_{0,1} \cdot N_{ft,1} / N_{st,1} = 0,00685$  where  $N_{ft,1} = 26$  is the total number of failure points.

The sampling region is next increased by multiplying each (negative) principal curvature  $k_i = 2\lambda_i$  ( $i=1, \dots, 18$ ) by a factor 1.1 and Equ. (20) is used to calculate the corresponding failure probability as  $P_{0,2} = 0.0085$ . The number of additional points to be sampled from the region bounded by the original and the new sampling functions,  $N_{sa,2}$ , is then determined as:  $N_{sa,2} = N_{st,1} (P_{0,2} - P_{0,1}) / P_{0,1} = 7$ . After additional seven points are sampled, the failure probability is updated as:  $P_{f,2} = P_{0,2} \cdot N_{ft,2} / N_{st,2} = 0.00689$  where  $N_{st,2} = N_{st,1} + N_{sa,2} = 37$  is the total number of sampled points and  $N_{ft,2} = 30$  the total number of failure points. The sampling region had to be deformed one more time before convergence was achieved yielding  $P_f = 0.00688$ . Convergence is assumed to be achieved when the magnitude of the relative change in the failure probability between two adjacent AIS iterations is less than 0.02.

Finally, to remove a potential error associated with determination of the initial MPP,  $u^*$ , the sampling region is increased by reducing  $\beta$  by 5% and the AIS procedure outlined above repeated until convergence of the failure probability is reached. The final solution  $P_f = 0.00689$  is obtained which is in a good agreement with the value 0.0064 obtained using the AMV+ method. As expected, the AIS-based value is somewhat larger since the method is deliberately made more conservative in order to ensure that the AIS sampling region fully covers the failure region.

#### IV. CONCLUSION

Based on the results obtained in the present study the following main conclusions can be drawn:

1. As a result of shrink fitting a gun-barrel steel jacket over the  $\alpha$ -SiC lining, the lining develops a triaxial compressive stress state almost over its entire length.

However, due to slippage at the lining/jacket interface, a substantial reduction in the magnitude of the compressive axial stress takes place near the free end of the barrel.

2. The observed reduction in the magnitude of the compressive axial stress in the lining enhance probability for lining failure by formation and growth of circumferential cracks near the barrel end during burst firing.

3. The probability for failure by formation and growth of circumferential cracks at the lining/jacket interface can be estimated relatively accurately using either the approximate analytical (the Advanced Mean Value) or a direct sampling (the Adaptive Importance Sampling) method at a substantially savings of the computational effort relative to that needed in the conventional Monte Carlo method.

## **V. ACKNOWLEDGEMENTS**

The material presented here is based on work supported by the U.S. Army Grant Number DAAH04-96-1-0197. The authors are indebted to Drs. Walter Roy, Fred Stenton and Bonnie Gersten of ARL for the continuing interest in the present work. The authors also acknowledge the support of the Office of High Performance Computing Facilities at Clemson University.



## REFERENCES

1. "Application of Nonconventional Materials to Guns and Gun Tubes", National Materials Advisory Board, National Research Council, NMAB-423 National Academy Press (1986).
2. J. J. Stiglich and R. N. Katz, "A Selected History of Gun Barrel Liner Materials Development", Sagamore Workshop on Gun Tube Wear and Erosion, Dupont Country Club, Wilmington, DE, 29-31 July (1996).
3. R. N. Katz, *Ceramic Eng. and Sci. Proceedings*, 4 (1983) 475.
4. R. N. Katz, "Ceramic Gun Barrel Liners: Retrospect and Prospect", US Army Research Laboratory, Sagamore Workshop on Gun Tube Wear and Erosion, Dupont Country Club, Wilmington, DE, 29-31 July (1996).
5. M. Gruzicic, J. R. DeLong and W. DeRosset, "Reliability Analysis of Hybrid Ceramic/Steel Gun Barrels", Materials Science and Engineering A, submitted for publication, December, , 2001.
6. H. R. Millwater and Y.-T. Wu, "Computational Structural Reliability Analysis of a Turbine Blade," Proceedings International Gas Turbine and Aeroengine Congress and Exposition, Cincinnati, OH, May 24-27, 1993.
7. Millwater, H.R., Y.-T. Wu, "Global/Local Methods for Probabilistic Structural analysis," AIAA/ASME Adaptive Structures Forum, La Jolla, CA, April 19-22, 1993.
8. H. R. Millwater, Y.-T. Wu and A. F. Fossum "Probabilistic Analysis of a Materially Nonlinear Structure," AIAA/ASME/ASCE/AHS/ASC Structural Dynamics and Materials Conference, Long Beach, CA, April 2-4, 1990.
9. H. R. Millwater, A.J. Smalley, Y.-T. Wu, T.Y. Torng and B.F. Evans "Computational Techniques for Probabilistic Analysis of Turbomachinery," ASME, International Gas Turbine and Aeroengine Congress and Exposition, Cologne, Germany, June 1-4, 1992.
10. T. Torng, Y.-T. Wu and H. R., Millwater, "Structural System Reliability Calculation Using a Probabilistic Fault Tree Analysis Method," AIAA/ASME/AHS/ASC Structures, Structural Dynamics and Materials Conference, Dallas, TX, April 13-15, 1992.
11. Y.-T. Wu, H. R. Millwater, and T. A. Cruse, "An Advanced Probabilistic Structural Analysis Method for Implicit Performance Functions," *AIAA Journal*, 28, (1990) 1663.
12. H. O. Madsen, S. Krenk, and N. C. Lind, "Methods of Structural Safety", Prentice-Hall, Inc., Englewood Cliffs, NJ, 1986.
13. R. Rackwitz and B. Fiessler, "Structural Reliability Under Combined Load Sequences," *Journal of Computers and Structures*, 9, (1978) 489.
14. Y.-T. Wu, T.Y. Torng, H.R. Millwater, A. F. Fossum and M. H. Rheinfurth, "Probabilistic Methods for Rotordynamics Analysis," presented at the 1991 SAE Conference, April, 1991.

15. K. Breitung, "Asymptotic Approximations for Probability Integrals," *Probabilistic Engineering Mechanics*, 4 (1989) 1.
16. P. Bjerager, "Probability Integration by Directional Simulation," *Journal of the Engineering Mechanics*, 114 (1987) 1.
17. ABAQUS/Standard User's Manual Version 5.8, Hibbitt, Karlesson, and Sorensen, Inc., Providence, RI, 1998.
18. Cambridge Engineering Selector, Version 3.1, Granta Design Ltd, Cambridge, UK, 2000.
19. R. N. Katz, Private Communication, 2001.
20. Sequential Simplex Optimization. A Technique for Improving Quality and Productivity in Research, Development, and Manufacturing. by Walters, Parker, Morgan and Deming, CRC Press, 1991.
21. A. H.-S. Ang and W. H. Tang, "Probability Concept in Engineering Planning and Design, Volume II: Decision, Risk, and Reliability", New York, John Wiley & Sons, Inc., 1984.
22. K. Breitung, "Approximations for Probability Integrals", *Probability Engineering Mechanics*, 4 (1989) 1.
23. H. R. Millwater and Y.-T. Wu, "Computational Structural Reliability Analysis of a Turbine Blade," Proceedings International Gas Turbine and Aeroengine Congress and Exposition, Cincinnati, OH, May 24-27, 1993.
24. W. Weibull, "A Statistical Theory of the Strength of Materials," *Ingeniors Vetenskaps Akademien Handlingar*, 151 (1939) 1.
25. N. N. Nemeth, J. M. Manderscheid and J. P. Gyekenyesi, "Ceramic Analysis and Reliability Evaluation of Structures (CARES)", *NASA*, TP-2919 (1990) 1.

**Table 1. Required Number of Function Evaluations in the Mean Value (MV), the Advanced Mean Value (AMV) and the Advance Mean Value with Iterations (AMV+) Procedures for a System with  $n$  Random Design Variables**

<b>Purpose</b>	<b>MV</b>	<b>AMV</b>	<b>AMV+</b>
<b>To Develop an MV-based Linearized Response Function, <math>Z_{MV}</math></b>	<b><math>n+1</math></b>	<b><math>n+1</math></b>	<b><math>n+1</math></b>
<b>To Compute the System Response at the MPP for a Selected Level of CDF</b>		<b>+1</b>	<b>+1</b>
<b>To Develop an MPP-based Linearized Response Function, <math>Z_{MPP}</math></b>			<b><math>+n+1</math></b>
<b>Total Number of Function Evaluations</b>	<b><math>n+1</math></b>	<b><math>n+2</math></b>	<b><math>2n+3</math></b>

**Table 2. Thermal and Mechanical Properties of  $\alpha$ -SiC and CrMoV Gun Barrel Steel and Process Parameters Used in the Present Finite Element Analysis**

Property	Symbol	Unit	Material			
			$\alpha$ -SiC		CrMoV Steel	
			Mean	Std. Dev.	Mean	Std. Dev.
Density	$\rho$	$kg / m^3$	3,170.0	50.0	7,850.0	50.0
Specific Heat	$c_p$	$J / kg \cdot K$	890.0	55.0	463.0	21.0
Thermal Conductivity	$k$	$W / m \cdot K$	134.0	26.0	54.6	5.5
Convective Heat Transfer Coefficient	$h$	$W / m^2 \cdot K$	135.0	22.0	190.0	14.0
Emissivity	$\varepsilon$	N/A	0.82	0.07	0.55	0.12
Coefficient of Linear Thermal Expansion	$\alpha$	$10^{-6} / K$	3.7	0.2	14.2	0.7
Young's Modulus	$E$	GPa	415.0	25.0	210.0	2.5
Poisson's Ratio	$\nu$	N/A	0.21	0.02	0.290	0.003
Tensile Strength	$\sigma_f$	MPa	700.0	0.0 *	1,070.0	70.0
$\alpha$ -SiC/CrMoV Steel Friction Coefficient	$\mu$	N/A	0.3	0.1	0.3	0.1
Initial Temperature	$T_0$	K	298.0	0.0 *	1,173.0	15.0

\* Zero value of the standard deviation indicates that the parameter in question is not considered as a random variable.

**Table 3.  $Z_{MV}$  Coefficients  $a_i$  in Equ. (3) and the Corresponding Sensitivities  $\alpha_i$ .**

Parameter Name	Random Variable	$a_i^*$	$\alpha_i$ at MV
Density of $\alpha$ -SiC	$X_1$	$0.00000 \cdot 10^{-0}$	$0.00000 \cdot 10^{-0}$
Specific Heat of $\alpha$ -SiC	$X_2$	$6.54545 \cdot 10^{-8}$	$-1.97563 \cdot 10^{-3}$
Thermal Conductivity of $\alpha$ -SiC	$X_3$	$1.99615 \cdot 10^{-6}$	$-2.84821 \cdot 10^{-2}$
Heat Transfer Coefficient of $\alpha$ -SiC	$X_4$	$-1.36364 \cdot 10^{-7}$	$1.64636 \cdot 10^{-3}$
Emissivity of $\alpha$ -SiC	$X_5$	$-1.42857 \cdot 10^{-6}$	$5.48787 \cdot 10^{-5}$
Thermal Expansion Coefficient of $\alpha$ -SiC	$X_6$	$0.00000 \cdot 10^{-0}$	$0.00000 \cdot 10^{-0}$
Young's Modulus of $\alpha$ -SiC	$X_7$	$-3.52800 \cdot 10^{-6}$	$4.84030 \cdot 10^{-2}$
Poisson's Ratio of $\alpha$ -SiC	$X_8$	$6.70000 \cdot 10^{-4}$	$-7.35375 \cdot 10^{-3}$
$\alpha$ -SiC/CrMoV Steel Friction Coefficient	$X_9$	$-1.54610 \cdot 10^{-2}$	$8.48480 \cdot 10^{-1}$
Density of CrMoV Steel	$X_{10}$	$2.40000 \cdot 10^{-8}$	$-6.58545 \cdot 10^{-4}$
Specific Heat of CrMoV Steel	$X_{11}$	$2.23810 \cdot 10^{-7}$	$-2.57930 \cdot 10^{-3}$
Thermal Conductivity of CrMoV Steel	$X_{12}$	$-6.72727 \cdot 10^{-7}$	$2.03051 \cdot 10^{-3}$
Heat Transfer Coefficient of CrMoV Steel	$X_{13}$	$-5.00000 \cdot 10^{-7}$	$3.84151 \cdot 10^{-3}$
Emissivity of CrMoV Steel	$X_{14}$	$-6.66667 \cdot 10^{-6}$	$4.39030 \cdot 10^{-4}$
Thermal Expansion Coefficient of CrMoV Steel	$X_{15}$	$-1.97857 \cdot 10^{-4}$	$7.60070 \cdot 10^{-2}$
Young's Modulus of CrMoV Steel	$X_{16}$	$-6.68000 \cdot 10^{-6}$	$9.16475 \cdot 10^{-3}$
Poisson's Ratio of CrMoV Steel	$X_{17}$	$7.66667 \cdot 10^{-4}$	$-1.26221 \cdot 10^{-3}$
Tensile Strength of CrMoV Steel	$X_{18}$	$-1.39000 \cdot 10^{-6}$	$5.33970 \cdot 10^{-2}$
Initial Temperature of CrMoV Steel	$X_{19}$	$1.40000 \cdot 10^{-7}$	$-1.15245 \cdot 10^{-3}$

\*  $a_0 = .01587900$

## FIGURE CAPTIONS

**Figure 1.** A schematic of the Most Probable Point Locus (MPPL) in a two random-variable space.

**Figure 2.** A schematic of the Adaptive Importance Sampling method in a two standard-normal random-variable space.

**Figure 3.** A schematic of the hybrid ceramic/steel gun barrel.

**Figure 4.** Models for: (a) thermal and (b) mechanical analyses and (c) the finite element mesh used in the present work.

**Figure 5.** Temperature contour plots in the gun barrel at three different times during the shrink-fit process: (a)  $t = 0.01$  sec, (b)  $t = 1$  sec, and (c)  $t = 100$  sec.

**Figure 6.** Distributions of: (a) the axial  $\sigma_{zz}$ ; (b) the radial  $\sigma_{rr}$ ; and (c) the circumferential  $\sigma_{\theta\theta}$  residual stresses in the barrel at the completion of the shrink-fit process.

**Figure 7.** Evolution of the residual axial stress,  $\sigma_{rr}$ , during the shrink-fit process. The cooling times for (a)-(c) are identical to the ones in Figures 5(a)-(c).

**Figure 8.** Variation of the residual axial stress,  $\sigma_{rr}$ , within a layer of the  $\alpha$ -SiC lining adjacent to the lining/jacket interface with a distance from the barrel end.

**Figure 9.** Cumulative Distribution Function (CFD) for the failure probability of the ceramic lining: (a) Linear scale; (b) Normal-distribution scale.

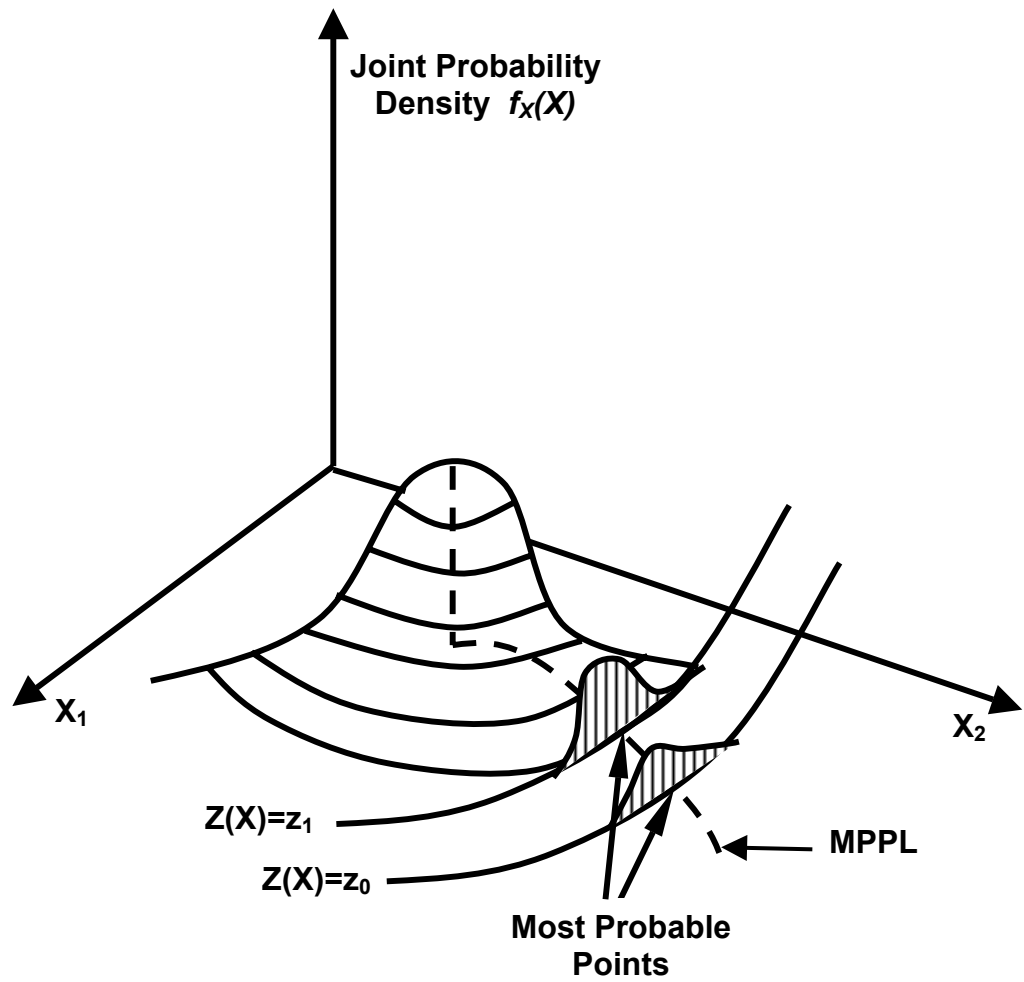


**Figure 1. A schematic of the Most Probable Point Locus (MPPL) in a two random-variable space.**

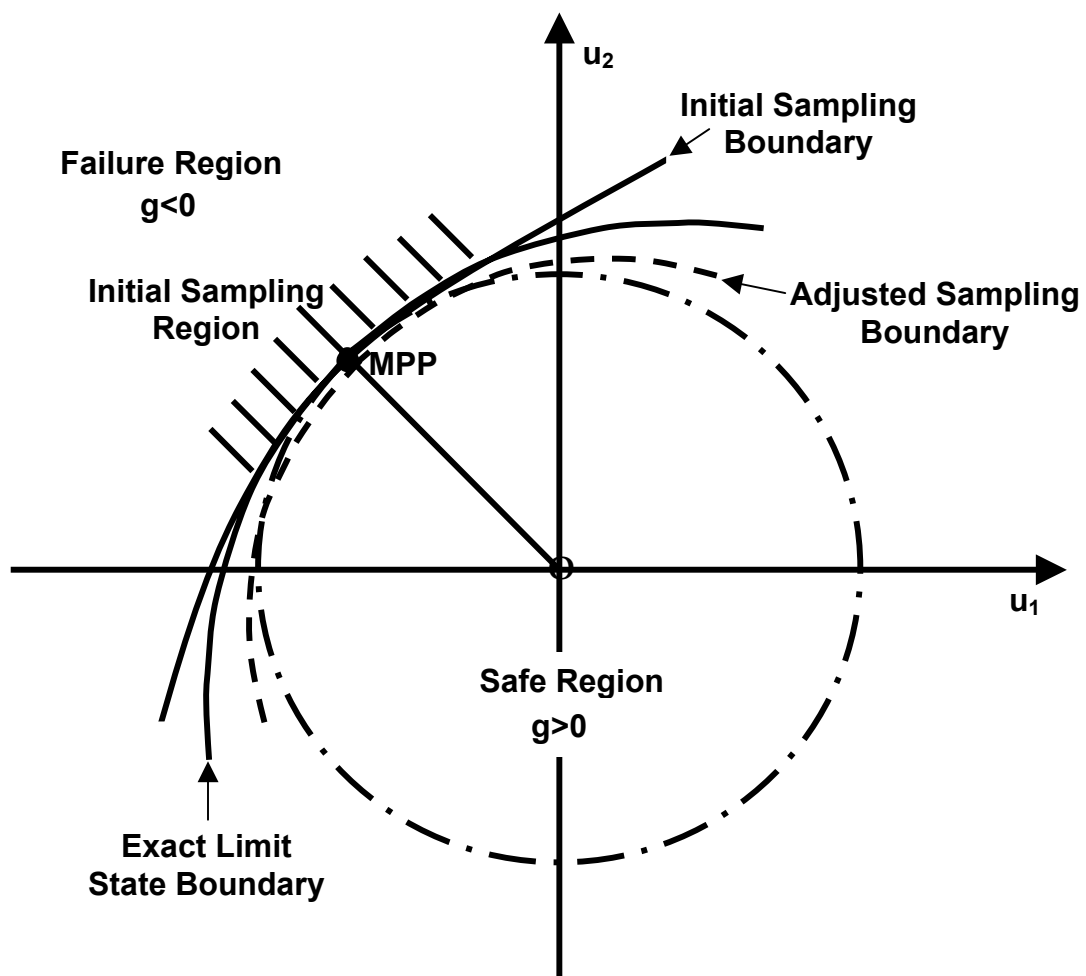
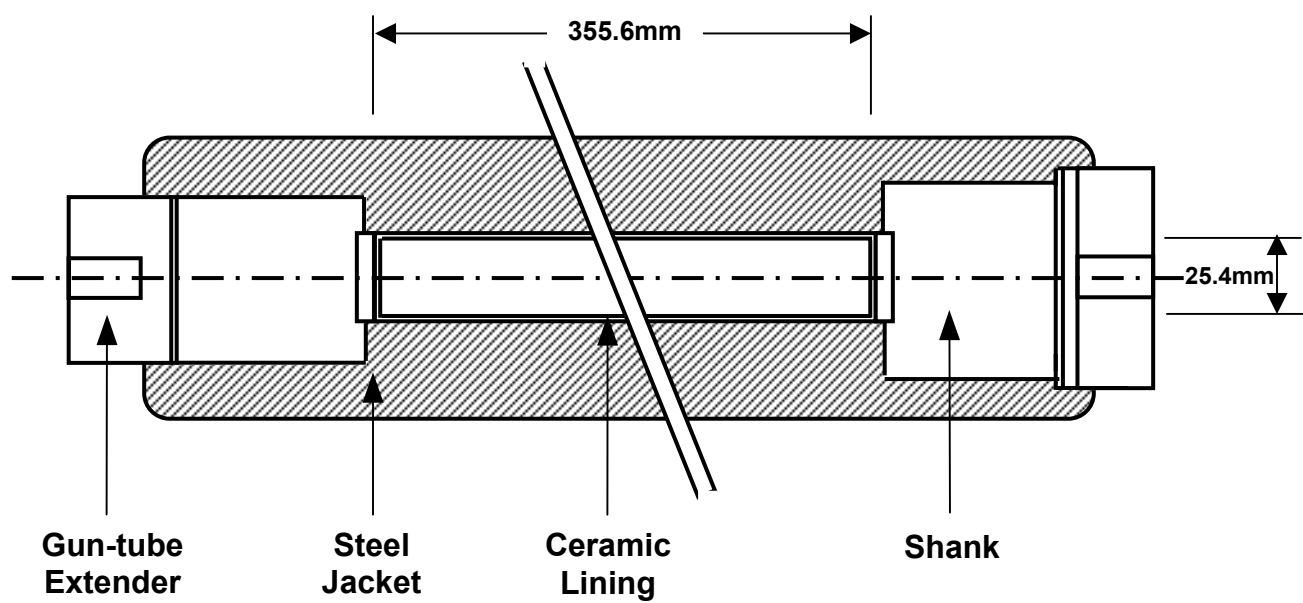
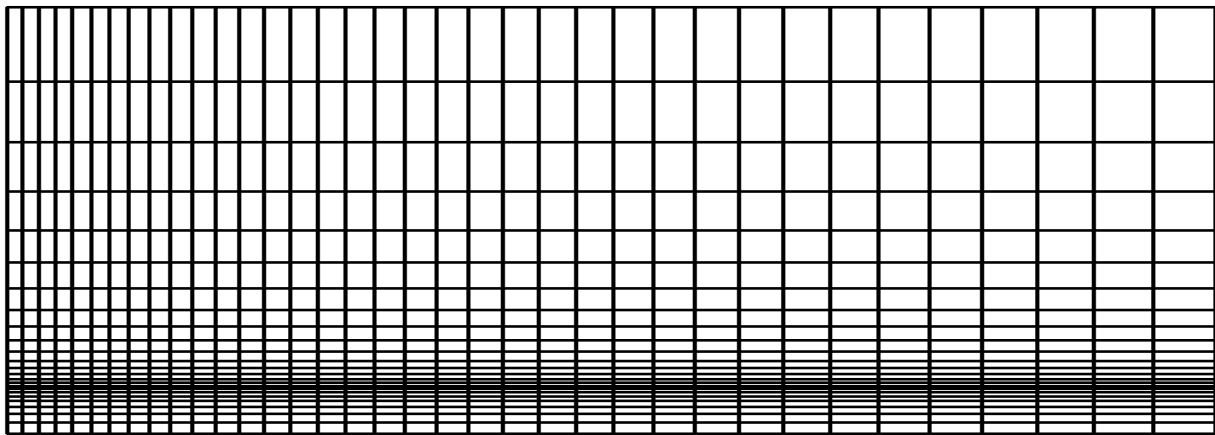
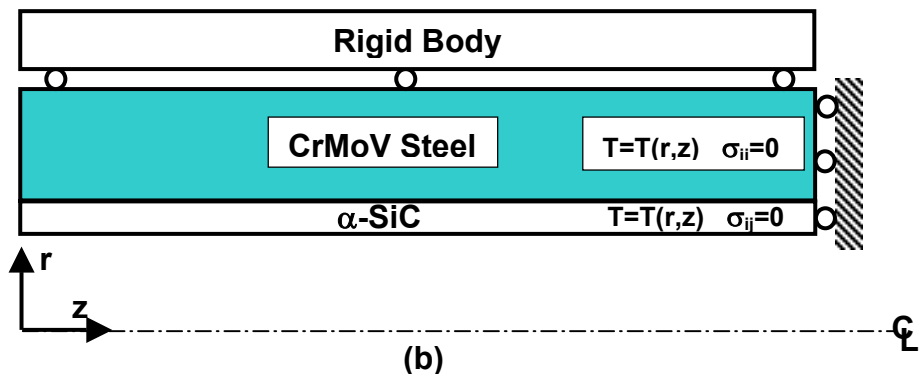
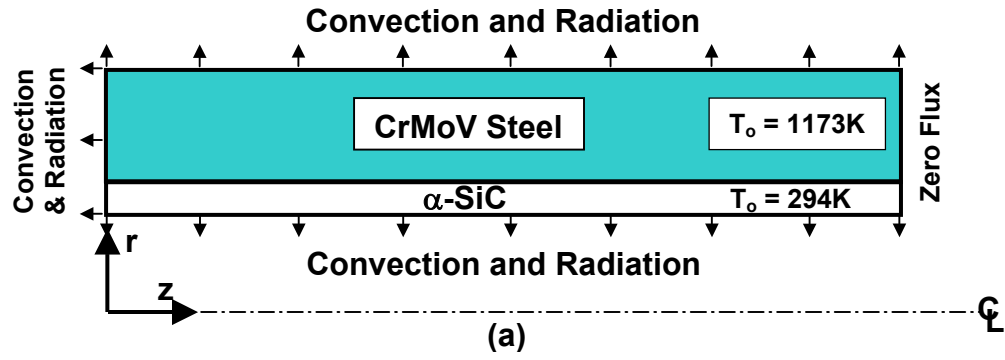


Figure 2. A schematic of the Adaptive Importance Sampling method in a two standard-normal random-variable space.





**Figure 3. A schematic of the hybrid ceramic/steel gun barrel.**



(c)

Figure 4. Models for: (a) thermal and (b) mechanical analyses and (c) the finite element mesh used in the present work.

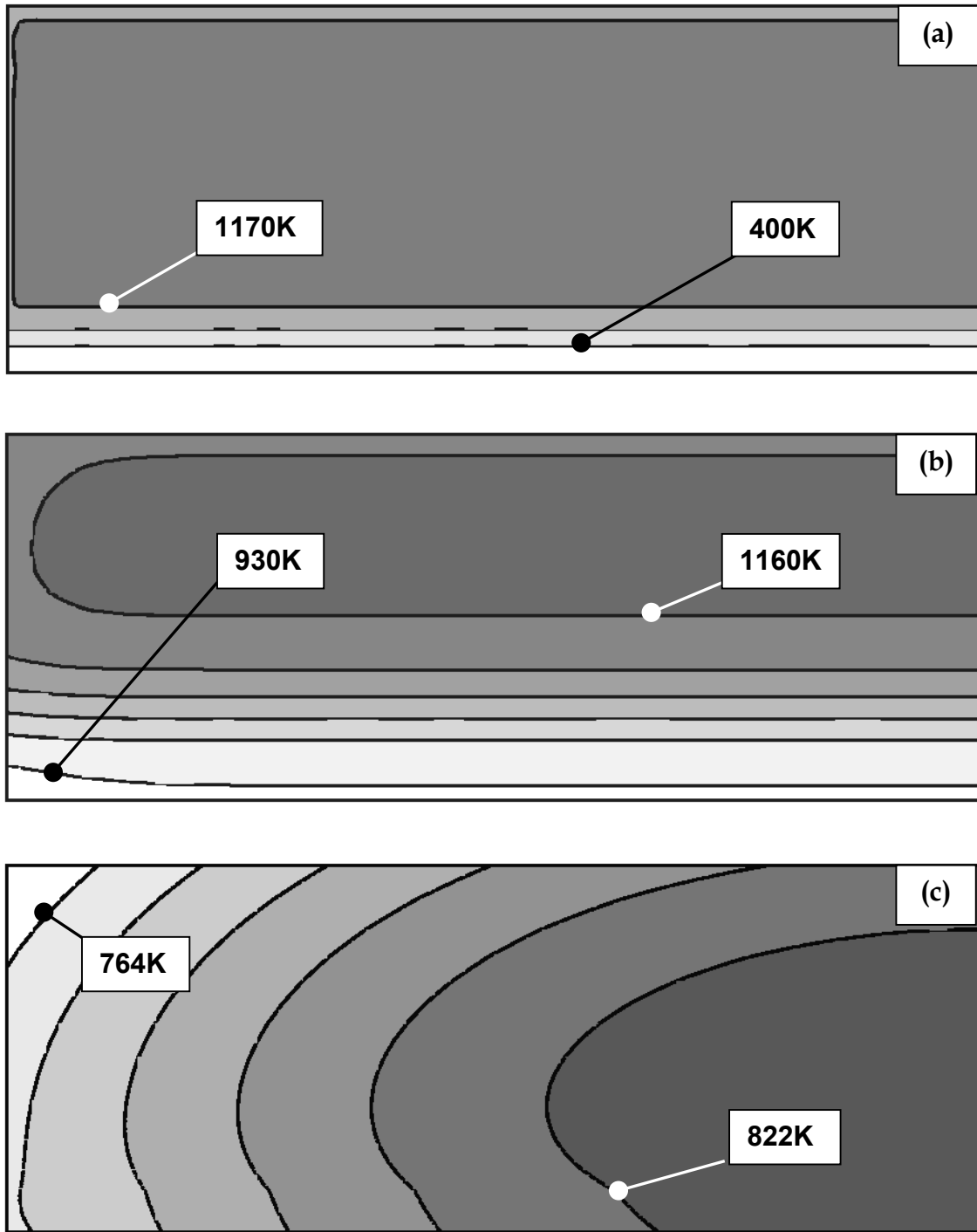


**Figure 5. Temperature contour plots in the gun barrel at three different times during the shrink-fit process: (a)  $t = 0.01$  sec, (b)  $t = 1$  sec, and (c)  $t = 100$  sec.**

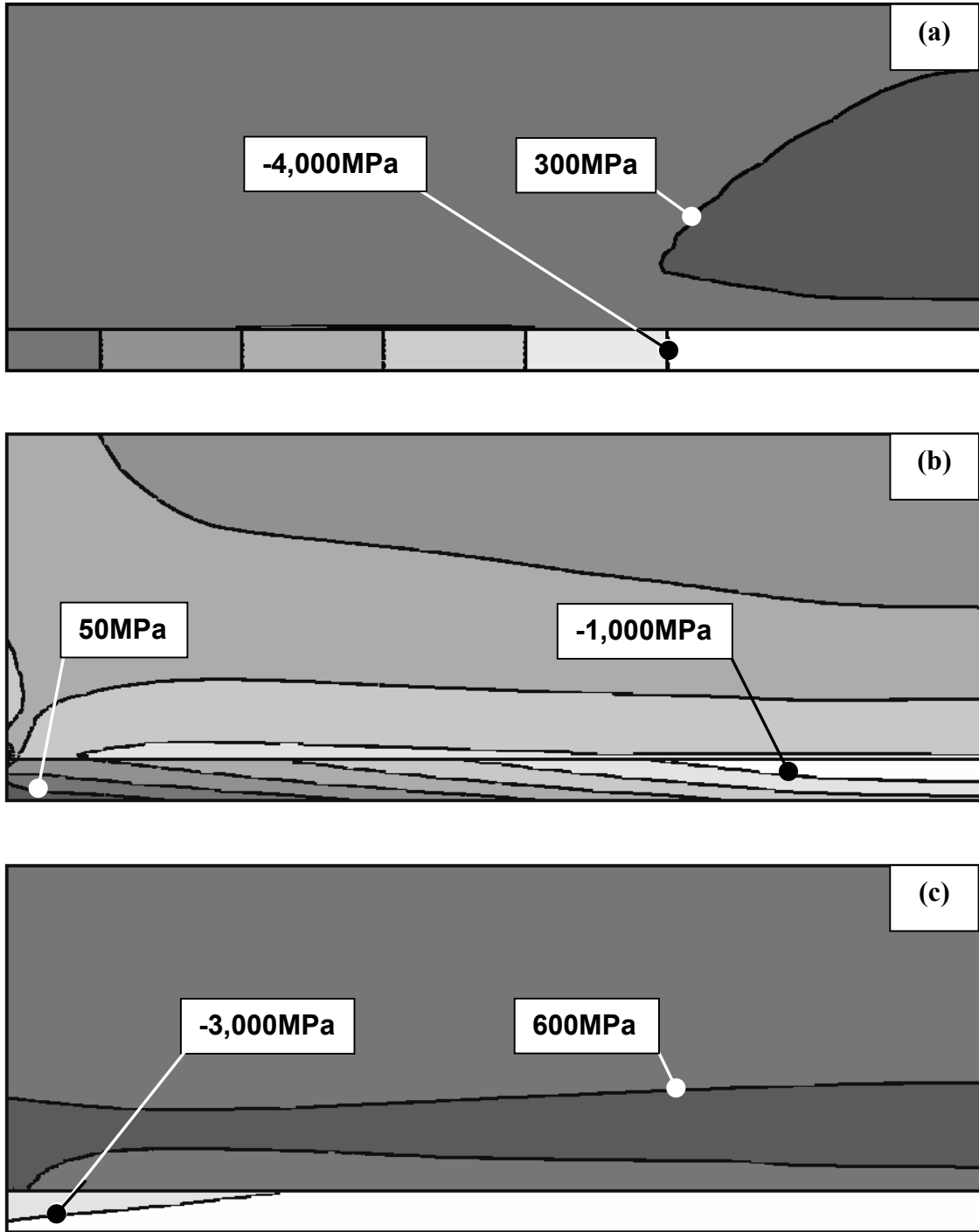


**Figure 6. Distributions of: (a) the axial  $\sigma_{zz}$ ; (b) the radial  $\sigma_{rr}$ ; and (c) the circumferential  $\sigma_{\theta\theta}$  residual stresses in the barrel at the completion of the shrink-fit process.**

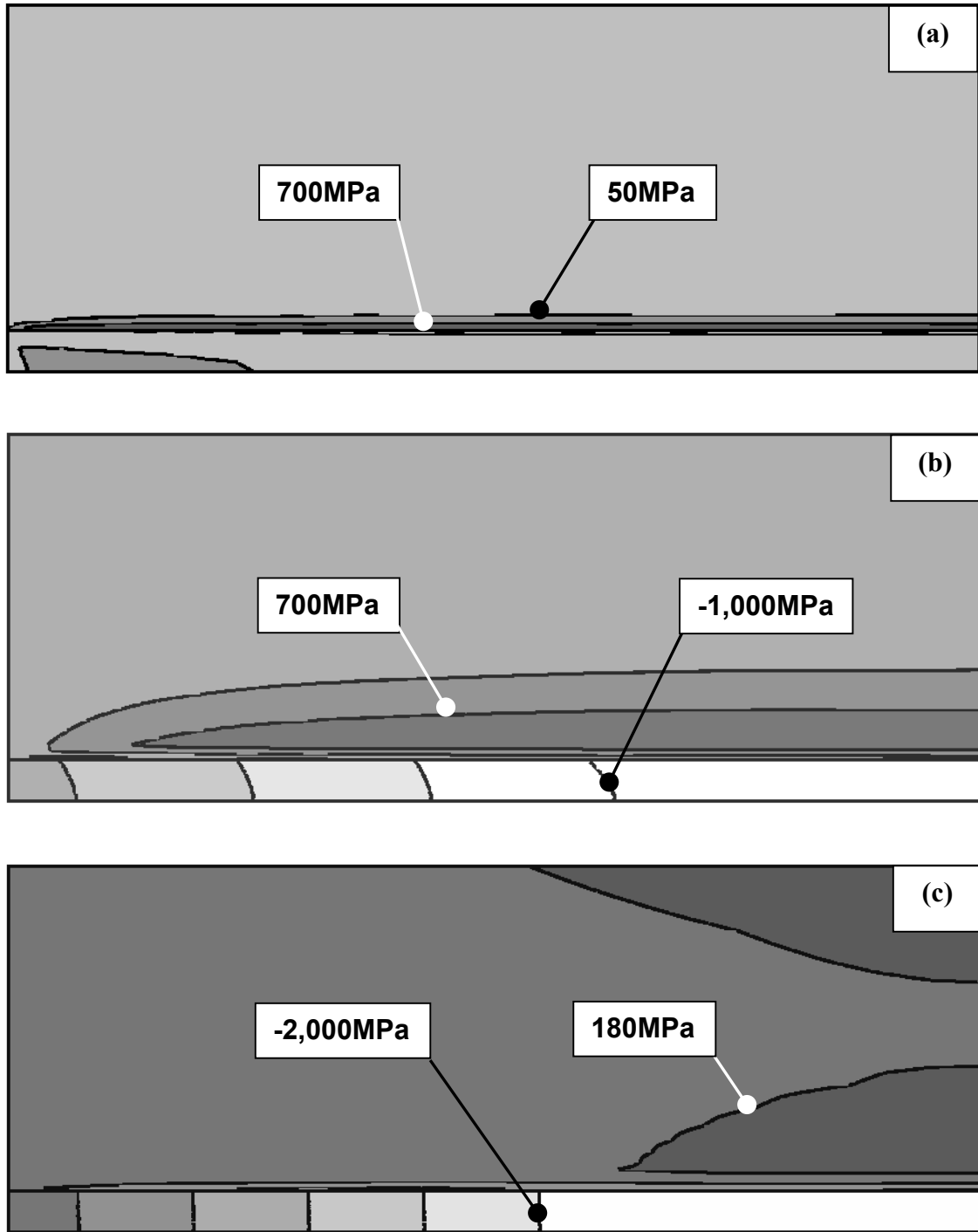


**Figure 7. Evolution of the residual axial stress,  $\sigma_{zz}$ , during the shrink-fit process. The cooling times for (a)-(c) are identical to the ones in Figures 5(a)-(c).**

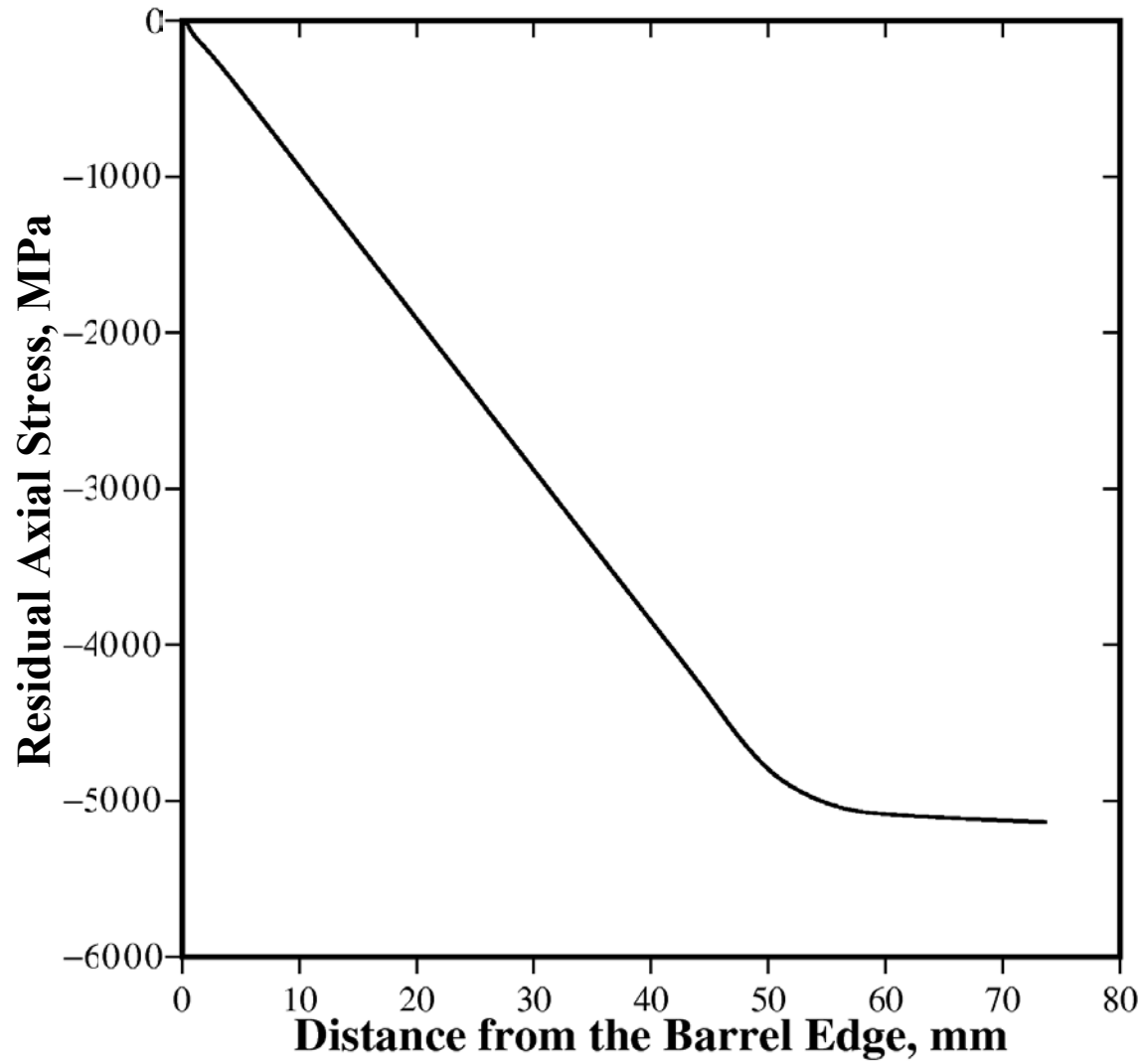


**Figure 8.** Variation of the residual axial stress,  $\sigma_{rr}$ , within a layer of the  $\alpha$ -SiC lining adjacent to the lining/jacket interface with a distance from the barrel end.

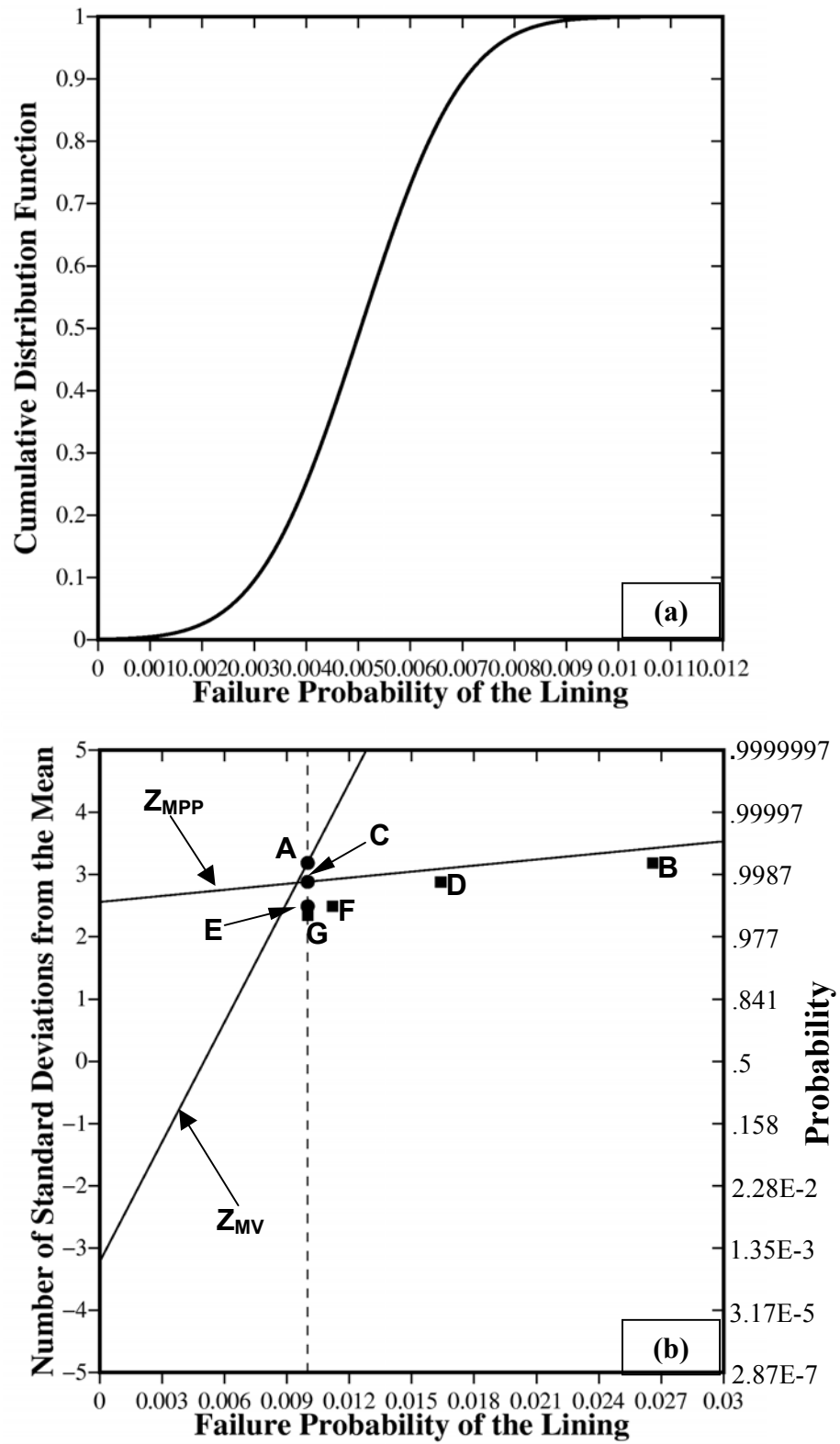


**Figure 9. Cumulative Distribution Function (CFD) for the failure probability of the ceramic lining: (a) Linear scale; (b) Normal-distribution scale.**